Deriving slope movements for an imminent landslide along the Jinsha River

Wentao Yang[1], Lianyou Liu[2,3,4], Peijun Shi[2,3,4]

[1]Three-gorges Reservoir Area (Chongqing) Forest Ecosystem Research Station, School of Soil and Water Conservation, Beijing Forestry University, Beijing, 100083, China
[2]Academy of Disaster Reduction and Emergency Management, Ministry of Emergency Management & Ministry of Education, Beijing Normal University, Beijing, 100875, China
[3]MOE, Key Laboratory of Environmental Change and Natural Disaster, Beijing Normal University, Beijing, 100875, China
[4]State Key Laboratory of Earth Surface Processes and Resource Ecology, Beijing Normal University, Beijing, 100875, China

Correspondence to: Lianyou Liu (lyliu@bnu.edu.cn) and Peijun Shi (spj@bnu.edu.cn)

Abstract. Landslides are major hazards that may pose serious threats to mountain communities. Even landslides in remote mountains could have non-negligible impacts on populous regions by blocking large rivers and forming megafloods. Usually, there are slope deformations before major landslides occur, and detecting precursors such as slope movement before major landslides occur is important for preventing possible disasters. In this work, we applied multi-temporal optical remote sensing images (Landsat 7 and Sentinel-2) and an image correlation method to detect sub-pixel slope deformations of a slope. Near the Mindu town in the Tibet Autonomous Region, this slope is also located along the Jinsha River, ~80km downstream the famous Baige landslide. We used DEM derived aspect to restrain background noises in image correlation results. We found the slope remained stable from November 2015 to November 2018 and moved significantly from November 2018 to November 2019. We used more data to analyse slope movement in 2019 and found retrogressive slope movements with increasingly large deformations near the river bank. We also analysed spatial-temporal patterns of the slope deformation from October 2018 to February 2020 and found seasonal variations in slope deformations. Only the slope foot moved in dry seasons, whereas the entire slope activated in rainy seasons. Until 24 August 2019, the size of the slope with displacements larger than 3 m is similar to that of the Baige landslide. However, the river width at the foot of this slope is much narrower than the river width at the foot of the Baige landslide. We speculate it may continue to slide down and dam the Jinsha River. Further modelling works should be done to check if the imminent landslide could dam the Jinsha River and measures be taken to mitigate possible dammed breach flood disasters. This work illustrates the potential of using optical remote sensing to monitor slope deformations over large remote mountain regions.

1 Introduction

Landslides are major natural hazards in mountain regions and have been causing widespread disasters every year around the globe (Petley 2012; Zhang et al. 2020). Major landslides in remote mountain regions may pose serious threats to downstream communities by choking channels to increase risks of landslide-dammed lake outburst floods (Fan et al. 2020;

Liu et al. 2019). For example, a hillslope near the Baige village had two landslides, damming the Jinsha River twice in 2018. The outburst floods caused widespread damage along its route and affected as far as Yunnan Province, > 500km from the landslides (Fan et al. 2019). In 2000, a super-large landslide dammed the Yigong River in Tibet and the outburst flood two

35 months later caused widespread damages, including 5 main bridges, highways and communication cables in downstream areas (Shang et al. 2013). The breach of the 1786 landslide-dammed lake in the Dadu river consumed >100,000 lives along its route (Dai et al. 2005). Similar cases occur in many mountain regions in the world and detecting precursors (such as slope movement) before major landslides is crucial for preventing such disasters (Intrieri et al. 2018; Carlà et al. 2019).

Remote sensing techniques have been an efficient way to monitor slope movement over large mountain regions (Du

40 et al. 2020; Handwerger et al. 2019). Optical passive and microwave active radar remote sensing most frequently used tools to detect slope displacements. There are two kinds of mainstream methods to derive slope movement. SAR interferometry processing use the difference in phase images to derive subtle slope movement of a few millimetres (Intrieri et al. 2018; Samsonov et al. 2020). However, large ground displacements (e.g., a few metres), dense vegetation or long time intervals could lead to incoherence in phase images in this types of methods (Wasowski and Bovenga 2014). Image correlation methods

45 (also referred as the pixel offset tracking) is another type of methods that use SAR amplitude or optical images to cross-correlating image patches to measure slope movement, which can derive sub-pixel ground displacements from 1/10 ~ 1/30 of a pixel (Li et al. 2020). The later type of methods are good at detecting larger slope movements that are visible on images (Bradley et al. 2019; Lacroix et al. 2020). In recent years, image correlation methods have been proposed and widely used to detect sub-pixel slope displacements in optical images (Bontemps et al. 2018; Lacroix et al. 2019; Lacroix et al. 2018; Yang

50 et al. 2020).

In this work, using sub-pixel optical image correlation methods we report a landslide along the Jinsha River. Different from previous retrospective studies, the landslide in this work did not collapse yet. We speculate that the slope is unstable and could pose a threat to downstream areas by blocking the Jinsha River. To test this hypothesis, we used multi-temporal Sentinel-2 images to detect possible slope displacements. We first used two Sentinel-2 images to find the relatively stable period before

55 the flood caused by the upstream Baige landslide (October and November 2018). Then, we further analysed the movement of the slope after the flood from the Baige landslide in 2019.

2 Methods

2.1 Study Area

The reported slope is ~80 km downstream the Baige landslide (Fan et al. 2019) along the Jinsha River near Mindu

60 town, Tibet Autonomous Region, bordering Sichuan Province (Figure 1a). The slope is located on the right bank of the Jinsha River. Similar to the Baige landslide, the geomorphology of this section of the Jinsha River is at the bottom of V-shaped valley. The elevation of the study area ranges from 2660m at the valley bottom to >4500m on the mountain ridge. This rough topography indicates strong fluvial incision against the rapid uplift of the Tibetan Plateau. We estimated the mean annual

precipitation (MAP) by using the GPM v6 monthly precipitation (from 2001 to 2019) and found the MAP of this area is ~665mm. The region is controlled by monsoon climate with >90% of the rain occurring from May to October. In addition, this area is tectonically active and active faults run through this slope from north to south. To the west of the faults are Upper Paleozoic strata, and to the east are Mesoproterozoic metamorphic rocks. Cracks and fissures on the slope is visible from the 15 m resolution pan-sharpened false colour Landsat 7 image acquired in 2001 (Figure 1b). These cracks and fissures may be relics of historic earthquakes or precipitations. This part of the slope has a percent slope of 45% and an aspect of the southeast, with azimuth between 112.5° and 157.5° (Figure 1c). This slope is mainly covered by grass and sparse shrubs and less affected by anthropogenic activities.

2.2 The COSI-Corr method

We mainly relied on Sentinel-2 optical images to derive slope movement. The European Space Agency's Sentienl-2 mission has two twine satellites in orbit, with a revisit time of less than 5 days. The Sentinel-2 optical imagery has 12 optical bands with wavelength ranging from 440nm to 2200nm. There are 4 bands with a spatial resolution of 10m: blue, green, red and near infrared bands. To derive slope movement, we used the red band because its wavelength is longer than other visible bands and is less influenced by the atmosphere. Compared to the near infrared, this band is less sensitive to vegetation and is more reliable to measure slope deformation (Yang et al. 2019). We used the Level-1C product, which is already orthorectified before distribution (Gascon et al. 2017).

This work used the COSI-Corr method, a correlation method for optical images, to detect slope displacements (Leprince et al. 2007). To derive slope movement, two image in a roll should be used to form an image pair, including the base image and the target image. The base image is an earlier image, based on which image correlation algorithm (here we use the COSI-Corr) is implemented to detect slope displacements in the target image (Leprince, et al. 2007). For detailed parameters to use the COSI-Corr method, please refer to Yang, et al. (2019b).

In this work, two steps were taken to detect slope displacements. First, we used two image pairs to detect slope movement before November 2018. For this step, we used three Sentinel-2 images on 13 November 2015, 12 November 2018 and 12 November 2019 to compose two image pairs. The first image pair is composed of a Sentinel-2 image on 13 November 2015 and a Sentinel-2 image on 12 November 2018. Sentinel-2 images of the second pair are acquired on 12 November 2018 and on 12 November 2019. Both image pairs are composed of Sentinel-2 images of similar dates of different years to minimize the influence of solar elevation angles (Yang et al. 2020).

We further used two image groups, a base image group and a target image group, to detect slope displacements and estimate uncertainties (Table 1). For the base image group, there are 19 images, all of which are acquired in early 2018. These selected 19 base images are clear images without clouds in 2018. Although Sentinel-2 images have very short revisit time, most images are contaminated by clouds on the Mindu slope before September 2018. For the target image group, we selected five images in 2019 (13 April, 17 July, 24 August, 5 October and 12 November) to detect slope displacements. For each target

image in 2019, average slope displacements and uncertainties are estimated from all 19 base images by forming 19 image pairs in the COSI-Corr method, separately. In all, there are 19×5 image pairs are calculated in the second step.

2.3 Error Assessment and postprocessing

There are some uncertainties in using image correlation methods, which may be caused by different viewing angles of images, different illuminations, et al. (Stmpf et al. 2016). The first two image pairs we mentioned above are composed by two images of very similar acquire dates of different years. Images of similar dates have similar zenith/elevation angles, which could minimize the influence of mountain shadows (Yang et al. 2020). In addition, misalignment between images can be estimated by selecting a stable zone (Bontemps et al. 2018; Lacroix et al. 2018; Yang et al. 2019). Mean displacements estimated within the stable zone will be used to correct image shifts. The stable zone in this work was selected on the upper part of the landslide (red rectangular in Fig 1b and 1c). We select this area because this stable zone is on the same slope as the landslide, which can minimize the influence of illumination and errors during orthorectification.

To derive spatial-temporal slope deformation patterns, we used nine images from 28 September 2018 to 7 February 2020 (Table 2) to form eight image pairs (periods) to derive slope displacements in different periods. All slope displacements were corrected by using the stable zone (the rectangular with red boundary in Figure 1b&1c). We further used the SRTM DEM derived aspect to filter out derived slope movement that does not agree with the aspect. If there are 15° deviations between the derived slope movement and the aspect, the derived slope movement is defined as not valid and will not be used for further analysis. This is reasonable for translational landslides as the mass moves downhill driven by gravity. Evidenced by optical images, the landslide in this work is a translational type and could be dealt with in this way (Highland and Bobrowsky 2013).

3 Results

3.1 Detected stable and unstable periods

In Table 3, The EW-mean and NS-mean indicate the shifts of images in both image pairs calculated from the stable zone. The EW-std and NS-std measures image distortions in the stable zone. Low EW-std and NS-std values indicates good performances during image orthorectifications. The derived EW-mean and NS-mean were then used to correct misalignment in images.

For image pair #1, the base image is acquired on 13 November 2015 and the second image is acquired on 12 November 2018. The slope remains stable in the first image pair, whereas detectable slope displacements can be found in the second image pair (Figure 2). The duration of the first image pair spans 3 years and the second image pair lasts one year. In Figure 2a, we can see that the slope displacement from 13 November 2015 to 12 November 2018 was less than 2 m, whereas there was more than 6 m slope displacement from 12 November 2018 to 12 November 2019 (Figure 2b). In image pair #2, larger displacements were observed near the Jinsha River and smaller displacements were farther away from the river. This increasing displacement magnitude may indicate the slope may start to move since its toe.

3.2 Slope displacements in 2019

As in Figure 2, we can see that the slope remains stable from November 2015 to November 2018 and is moving after November 2018. To derive time series of the Mindu slope displacements after November 2018, we used 19 base images in the stable period and 5 target images in 2019. All 19 base images are from early 2018, during which the slope was stable. Five selected target images are acquired on 13 April 2019, 17 July 2019, 24 August 2019, 5 October 2019 and 12 November 2019. For each target image in 2019, we calculated slope movement by using all base images. Therefore, there are 19 estimated slope displacements for each target image. We calculated the means and standard deviations of slope displacements for each target image representing slope movement from early 2018 and six periods in 2019 (Figure 3).

From Figure 3, we can see that the mean displacements are a magnitude larger than standard deviations, which indicate that the displacements derived between each target image and their base images agree with each other quite well. Minor slope displacements were detected until April 2019 (maximum 3~4m), whereas larger slope displacements can be observed in the later four target images (>5 m). All displacements in five target images show a similar pattern with results in image pair 2 (Figure 2b), demonstrated by larger displacements near the river and less movement further from the river. However, the third target image (24 August 2019) has more displacement of large values than other target images. As seen from Figure 3, it is quite possible that the slope moved significantly during 2019.

We further selected six points on the slope to analyse time series of the slope displacements in 2019 (Figure 4). For most target images in the first five points (p1-p5), most base images could derive >10 valid displacements (2-D columns). For all six points, accumulated displacements show similar growing trends from April 2019 to November 2019. Maximum displacements in all six points occurred on 24 August 2019. These unreasonably large values may be caused by difference of solar elevation/zenith angles in target images. For example, compared to the August image there are more mountain shadows in the November images in northern hemisphere. Despite abnormal displacements in August 2019, we can still see that displacements from July to November 2019 are still larger than displacements in April 2019. Therefore, from time series of these six points, we can see that major slope displacements occurred from April to August 2019.

3.3 Slope displacements in eight selected periods after November 2018

To analyse spatial deformation patterns in different periods, we selected 9 Sentinel-2 images forming eight image pairs (corresponding to eight periods in ~2 months). The first two image pairs (Figure 5a-b) shows that the middle and lower parts of the slope deformed significantly and 4-6 meters of displacement occurred at multiple locations. The study area has a monsoonal climate with most precipitation occurs from May to September (Figure 6). There are seasonal differences in deformation of this landslide. In dry seasons of winter and spring, deformation occurs at the foot of the slope near the Jinsha River and deformation rate is generally less than 1 m/month (from January to May, Figure 5c&d and periods 3-4 in Figure 6). In rainy seasons of summer and autumn, deformation affects the entire slope with some parts at a rate of more than 3 meters/month (from May to September, Figure 5e&f and periods 5-6 in Figure 6).

4 Discussion

160   Major landslides in mountains may dam river channels forming transient lakes, the breach of which can result in catastrophic floods to downstream communities (Dai et al. 2005; Fan et al. 2019; Liu et al. 2019). In this work, we examined a hillslope near Mindu town along the Jinsha River. We found the slope had significant movement from November 2018 to November 2019. Despite the area of the detected moving slope (715,577 m^2 for displacements larger than 3 m) is similar with the area of the Biage landslide (830,624 m^2), the width of the Jinsha River channel below the Mindu slope (~ 50) is half that
165   of the Baige (>100 m, in Figure 7). Considering the similar morphology of both river sections, the collapse of the Mindu slope may pose a threat to downstream communities by blocking the Jinsha River. We call for further frequent monitoring of the hillslope with other tools, such as InSAR (Intrieri et al. 2018; Samsonov et al. 2020).

There are a few strategies to suppress background noises in derived results, including selecting results with high signal/noise ratios (Lacroix et al. 2018; Yang et al. 2020), integrating redundant information in time series of images (Bontemps
170   et al. 2018). This work introduced a new method to use slope aspect to filter out slope movement that is different from the aspect. This procedure could eliminate false slope movements and reserves true slope movement of the Mindu landslide.

Many factors can influence the accuracy of slope deformation derivations by using image correlation methods, which includes errors during image orthorectification, different viewing angles of images, different illuminations, et al. (Stmpf et al. 2016; Yang et al. 2020). This work used Sentinel-2 L1C product, which is already orthorectified before distribution (Gascon
175   et al. 2017). To correct for possible mis-registration between base and master images, we used a stable zone to calculate image shifts. To reduce errors caused by different illuminations and viewing angles of images during acquisition, all images used for the first two Sentinel-2 image pairs are from similar dates of different years. To derive cumulative displacements, we used 19 base images in early 2018 to detect slope displacements in five target images in 2019.

5 Conclusions

180   By using image correlation technique, we can track sub-pixel slope movement in optical remote sensing images. We adopted an aspect constraint to automatically pick out downslope movement and significantly depressed much of the background noise. We applied these techniques on multi-temporal Sentinel-2 images to detect slope movement near the Mindu town along the Jinsha River. We found the Mindu landslide probably existed before 2001 and the slope remains relatively stable between November 2015 and November 2018. Significant slope displacements were observed from November 2018 to
185   August 2019.

We found the size of the Mindu slope that activated is similar to that of the Baige landslide, whereas the river width under the Mindu slope is half of the Baige section. If the Mindu landslide continues to slide down and occur, it may block the Jinsha River leading to similar social-economic consequences as the 2018 Baige landslide. However, optical images, such as the Sentinel-2 images, can only detect slope movements up to a few metres. To derive minor slope displacements, InSAR

techniques should be implemented for this remote slope. We also call for continuous monitoring of this slope and modelling of landslides caused river blocking and subsequent flooding.

Data availability. All Sentinel-2 images and the Landsat 8 image in this work were downloaded from the GEE. The SRTM DEM and its derivative were downloaded from the Geospatial Data Cloud website (http://www.gscloud.cn/sources).

Supplement. There is no related supplement for this paper.

Author contribution. LL and PS discovered the moving slope of this work. WY conducted analysis and drafted the manuscript.

Competing interests. The authors declare no conflict of interest.

Acknowledgement. WY would like to show his gratitude to his large family for catering his 2-year old daughter, while this work was underway.

Financial support. This work is jointly supported by the National Science Foundation of China (No. 41807500) and the Second Tibetan Plateau Scientific Expedition and Research Program (STEP), Grant No. 2019QZKK0902.

References

Bontemps, N., Lacroix, P., and Doin, M.-P.: Inversion of deformation fields time-series from optical images, and application to the long term kinematics of slow-moving landslides in Peru. Remote Sens. Environ., 210, 144-158, https://doi.org/10.1016/j.rse.2018.02.023, 2018.

Bradley, K., Mallick, R., Andikagumi, H., Hubbard, J., Meilianda, E., Switzer, A., Du, N., Brocard, G., Alfian, D., Benazir, B., Feng, G., Yun, S.-H., Majewski, J., Wei, S., and Hill, E.M.: Earthquake-triggered 2018 Palu Valley landslides enabled by wet rice cultivation. Nat. Geosci., 12, 935-939, https://doi.org/10.1038/s41561-019-0444-1, 2019.

Carlà, T., Intrieri, E., Raspini, F., Bardi, F., Farina, P., Ferretti, A., Colombo, D., Novali, F., and Casagli, N.: Perspectives on the prediction of catastrophic slope failures from satellite InSAR. Scientific Report, 9, 14137, https://doi.org/10.1038/s41598-019-50792-y, 2019.

Dai, F., Lee, C., Deng, J., and Tham, L.G.: The 1786 earthquake-triggered landslide dam and subsequent dam-break flood on the Dadu River, southwestern China. Geomorphology, 65, 205-221, https://doi.org/10.1016/j.geomorph.2004.08.011, 2005.

Du, J., Glade, T., Woldai, T., Chai, B., and Zeng, B.: Landslide susceptibility assessment based on an incomplete landslide inventory in the Jilong Valley, Tibet, Chinese Himalayas. Eng. Geol., 270, 105572, https://doi.org/10.1016/j.enggeo.2020.105572, 2020.

Fan, X., Dufresne, A., Subramanian, S.S., Strom, A., Hermanns, R., Stefanelli, C.T., Hewitt, K., Yunus, A.P., Dunning, S., Capra, L., Geertsema, M., Miller, B., Casagli, N., Jansen, J.D., and Xu, Q.: The formation and impact of landslide dams – State of the art. Earth-Science Reviews, 203, 103116, https://doi.org/10.1016/j.earscirev.2020.103116, 2020.

220   Fan, X., Xu, Q., Alonso-Rodriguez, A., Subramanian, S.S., Li, W., Zheng, G., Dong, X., and Huang, R.: Successive landsliding and damming of the Jinsha River in eastern Tibet, China: prime investigation, early warning, and emergency response. Landslides, 16, 1003-1020, https://doi.org/10.1007/s10346-019-01159-x, 2019.

Gascon, F., Bouzinac, C., Thépaut, O., Jung, M., Francesconi, B., Louis, J., Lonjou, V., Lafrance, B., Massera, S., Gaudel-Vacaresse, A., Languille, F., Alhammoud, B., Viallefont, F., Pflug, B., Bieniarz, J., Clerc, S., Pessiot, L., Trémas, T., Cadau,

225   E., De Bonis, R., Isola, C., Martimort, P., and Fernandez, V.: Copernicus Sentinel-2A Calibration and Products Validation Status. Remote Sens., 9(6), 584, https://doi.org/10.3390/rs9060584, 2017.

Handwerger, A.L., Fielding, E.J., Huang, M., Bennett, G.L., Liang, C., Schulz, W.H.: Widespread Initiation, Reactivation, and Acceleration of Landslides in the Northern California Coast Ranges due to Extreme Rainfall. J. Geophys Res-Earth, 124, 1782-1797, https://doi.org/10.1029/2019JF005035, 2019

230   Highland, L. and Bobrowsky, P.: The Landslide Handbook—a Guide to Understanding Landslides: A Landmark Publication for Landslide Education and Preparedness. Springer Berlin Heidelberg. 2013.

Intrieri, E., Raspini, F., Fumagalli, A., Lu, P., Del Conte, S., Farina, P., Allievi, J., Ferretti, A., and Casagli, N.: The Maoxian landslide as seen from space: detecting precursors of failure with Sentinel-1 data. Landslides, 15, 123-133, https://doi.org/10.1007/s10346-017-0915-7, 2018.

235   Lacroix, P., Araujo, G., Hollingsworth, J., and Taipe, E.: Self-Entrainment Motion of a Slow-Moving Landslide Inferred From Landsat-8 Time Series. J. Geophys Res-Earth, 124, 1201-1216, https://doi.org/10.1029/2018jf004920, 2019.

Lacroix, P., Berthier, E., and Maquerhua, E.T.: Earthquake-driven acceleration of slow-moving landslides in the Colca valley, Peru, detected from Pléiades images. Remote Sens. Environ., 165, 148-158, https://doi.org/10.1016/j.rse.2015.05.010, 2015.

Lacroix, P., Bièvre, G., Pathier, E., Kniess, U., and Jongmans, D.: Use of Sentinel-2 images for the detection of precursory

240   motions before landslide failures. Remote Sens. Environ., 215, 507-516, https://doi.org/10.1016/j.rse.2018.03.042, 2018.

Lacroix, P., Dehecq, A., and Taipe, E.: Irrigation-triggered landslides in a Peruvian desert caused by modern intensive farming. Nat. Geosci., 13, 56-60, https://doi.org/10.1038/s41561-019-0500-x, 2020.

Leprince, S., Barbot, S., Ayoub, F., and Avouac, J.: Automatic and Precise Orthorectification, Coregistration, and Subpixel Correlation of Satellite Images, Application to Ground Deformation Measurements. IEEE T. Geosci. Remote, 45, 1529-1558,

245   https://doi.org/10.1109/TGRS.2006.888937, 2007.

Li, M., Zhang, L., Ding, C., Li, W., Luo, H., Liao, M., and Xu, Q.: Retrieval of historical surface displacements of the Baige landslide from time-series SAR observations for retrospective analysis of the collapse event. Remote Sens. Environ., 240, 111695, https://doi.org/10.1016/j.rse.2020.111695, 2020.

Liu, W., Carling, P., Hu, K., Wang, H., Zhou, Z., Zhou, L., Liu, D., Lai, Z., and Zhang, X.: Outburst floods in China: A review.

250   Earth-Science Reviews, 197, 102895, https://doi.org/10.1016/j.earscirev.2019.102895, 2019.

Luo, S., Jin, X. and Huang, D.: Long-term coupled effects of hydrological factors on kinematic responses of a reactivated landslide in the Three Gorges Reservoir. Eng. Geol., 261, 105271, https://doi.org/10.1016/j.enggeo.2019.105271, 2019.

Petley, D.: Global patterns of loss of life from landslides. Geology, 40, 927-930, https://doi.org/10.1130/G33217.1, 2012.

Samsonov, S., Dille, A., Dewitte, O., Kervyn, F., and d'Oreye, N.: Satellite interferometry for mapping surface deformation time series in one, two and three dimensions: A new method illustrated on a slow-moving landslide. Eng. Geol., 266, 105471, https://doi.org/10.1016/j.enggeo.2019.105471, 2020.

Shang, Y., Yang, Z., Li, L., Liu, D., Liao, Q., and Wang, Y.: A super-large landslide in Tibet in 2000: background, occurrence, disaster, and origin. Geomorphology, 54(3-4), 225-243, https://doi.org/10.1016/S0169-555X(02)00358-6, 2003.

Stumpf, A., Malet, J.P., Puissant, A., and Travelletti, J.: Monitoring of Earth Surface Motion and Geomorphologic Processes by Optical Image Correlation. Land Surface Remote Sensing, 147-190, https://doi.org/10.1016/B978-1-78548-105-5.50005-0, 2016.

Wasowski, J. and Bovenga, F.: Investigating landslides and unstable slopes with satellite Multi Temporal Interferometry: Current issues and future perspectives. Eng. Geol., 174, 103-138, https://doi.org/10.1016/j.enggeo.2014.03.003, 2014.

Yang, W., Wang, Y., Sun, S., Wang, Y., and Ma, C.: Using Sentinel-2 time series to detect slope movement before the Jinsha River landslide. Landslides, 16, 1313-1324, doi: 10.1007/s10346-019-01178-8, 2019.

Yang, W., Wang, Y., Wang, Y., Ma, C., and Ma, Y.: Retrospective deformation of the Baige landslide using optical remote sensing images. Landslides, 17, 659-668, https://doi.org/10.1007/s10346-019-01311-7, 2020.

Zhang, S., Li, C., Zhang, L., Peng, M., Zhan, L., and Xu, Q.: Quantification of human vulnerability to earthquake-induced landslides using Bayesian network. Eng. Geol., 265, 105436, https://doi.org/10.1016/j.enggeo.2019.105436, 2020.
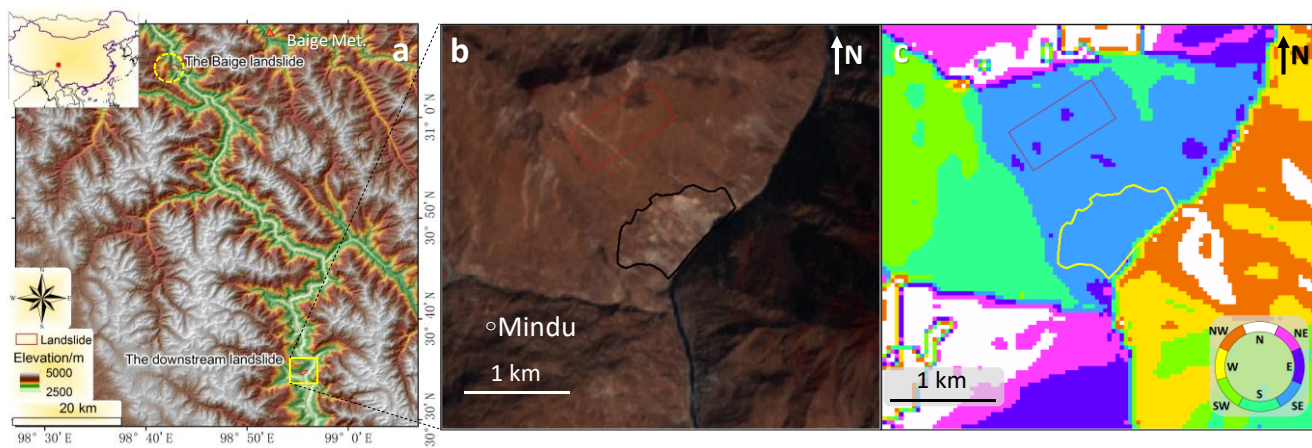
Figure 1: Topographic maps of the study area. (a) Geographic locations of the Baige landslide and the downstream landslide around the Mindu town, Tibet Autonomous Region. (b) A 15 m resolution pan-sharpened Landsat 7 false colour image on 18 February 2001 and (c) aspect of the study area around the Mindu landslide (The elevation data in a is a product of the NASA's Shuttle Radar Topography Mission (SRTM) and the aspect in c is a derivative of the DEM. The red polygons in b and c are the selected stable zone. Both the SRTM DEM in a and its derivative c are downloaded from the Geospatial Data Cloud website (http://www.gscloud.cn/sources). The Landsat image in b is a joint product of the USGS and NASA and was downloaded via the Google Earth Engine (GEE)).
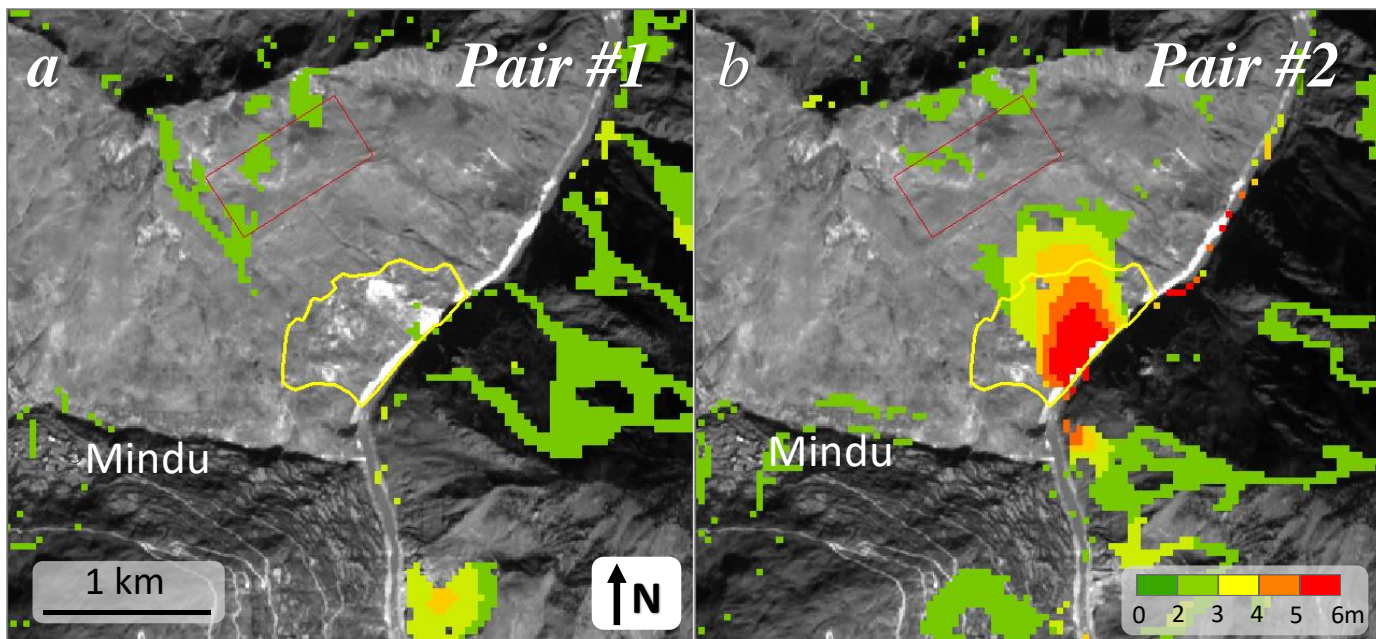
Figure 2: Detected slope displacements in image pairs #1 and #2 (Background Sentinel-2 images are acquired on 13 November 2015 and 12 November 2018, respectively. Both images were produced by the ESA's Sentinel-2 satellites and downloaded via the GEE).
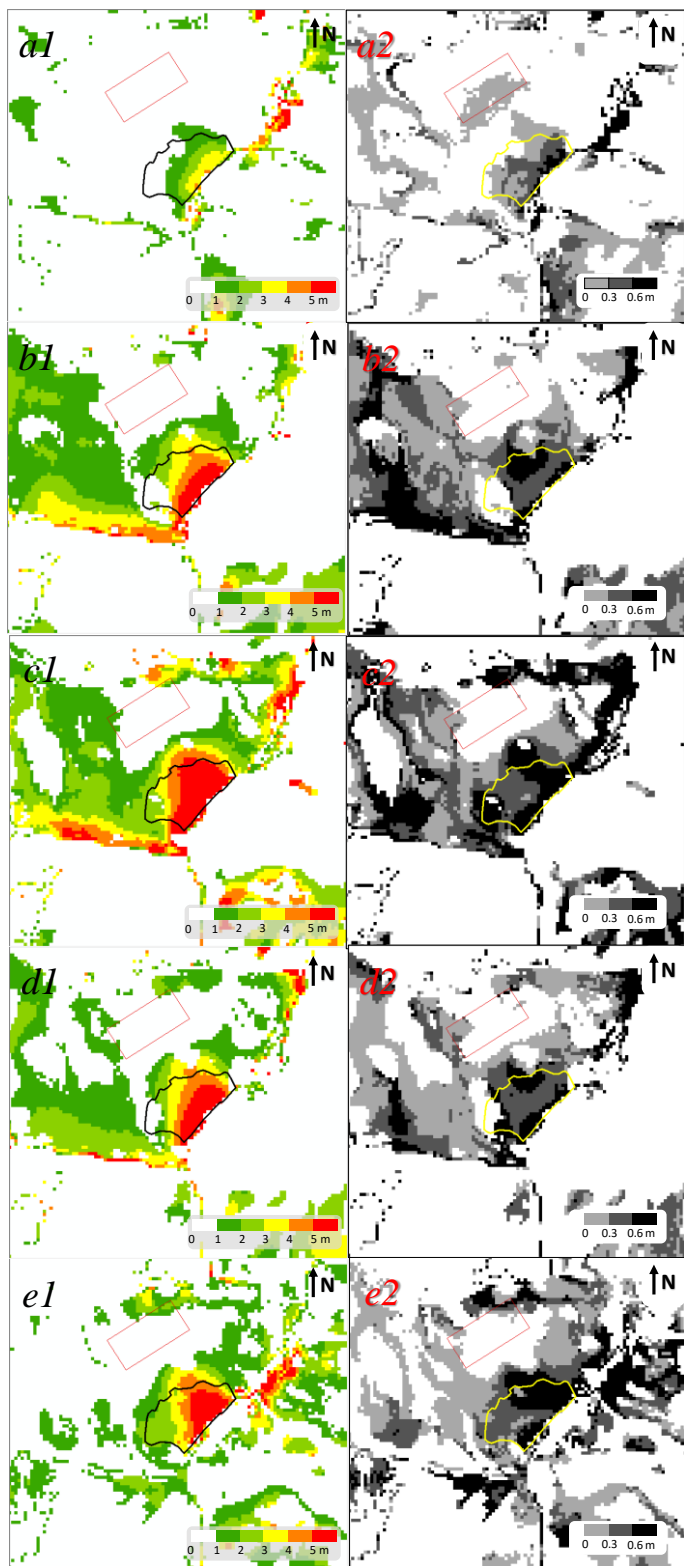
Figure 3: Means and standard deviations of derived slope displacements in nine targeted images (Tab. 2). Detected means and standard deviations of slope displacement on 13 Apr. 2019 (*a1-a2*), 17 Jul. 2019 (*b1-b2*), 24 Aug. 2019 (*c1-c2*), 5 Oct. 2019 (*d1-d2*), 12 Nov. 2019 (*e1-e2*), respectively.

285
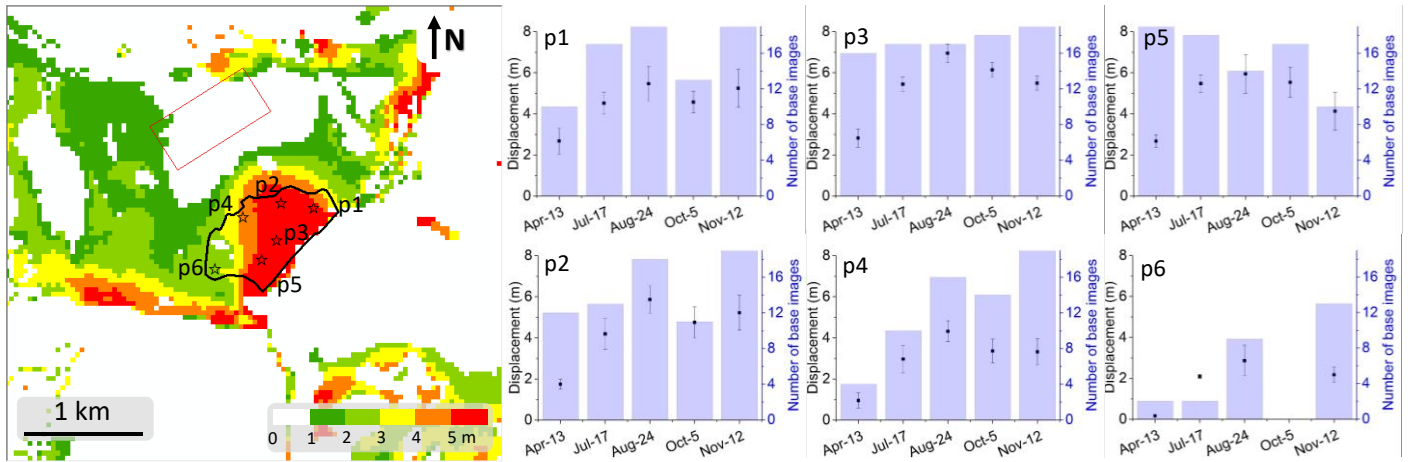
Figure 4: Time series of slope displacements for the six target images. Image to the left shows slope displacements shown above the Sentinel-2 image on 12 November 2019 and map colour is shown in minimum-maximum linear stretch type. Sub-panels p1-p6 show means (points), standard deviations (vertical bars) and valid numbers (histograms) of cumulative displacements between 19 base and 5 target images for the six selected points (stars) in the left image.
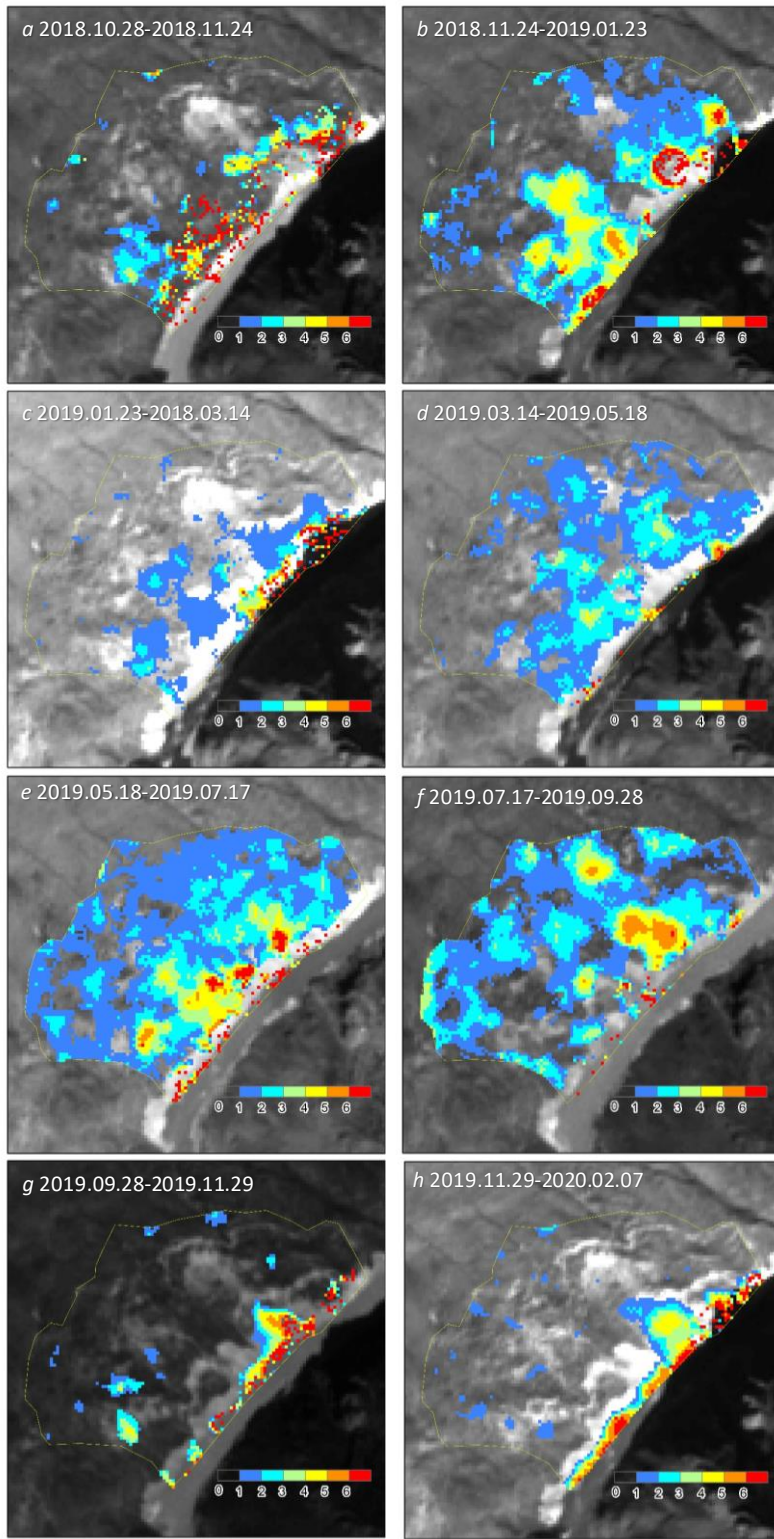
Figure 5: Slope displacements in different periods after the Baige floods (Background images are Sentinel-2 data produced by the ESA's Sentinel-2 satellites and downloaded via the GEE).

290
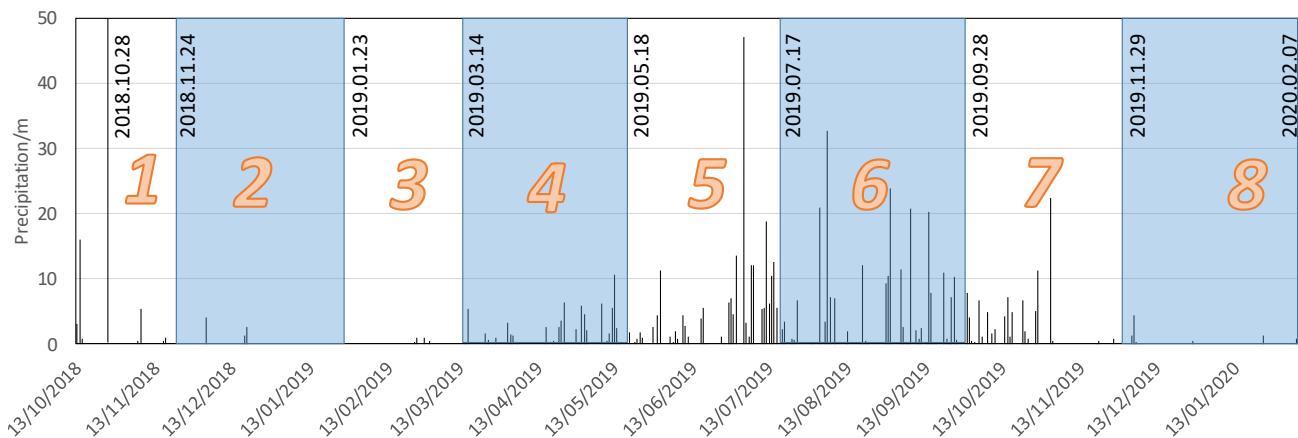
Figure 6: Daily precipitation of the Baiyu Meteorology station from October 2018 to February 2020.
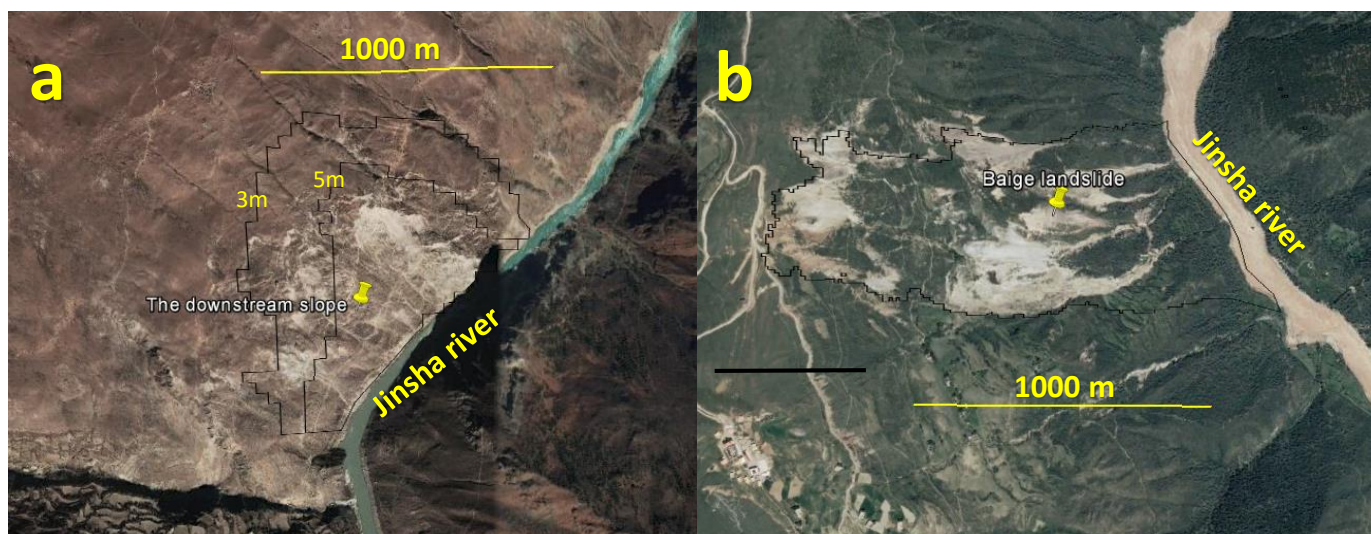
Figure 7: High spatial resolution images from the ©Google Earth. The image to the left is acquired on 30 March 2015 for the Mindu slope (a) and the right image is acquired on 18 July 2017 for the Baige slope (b).

Table 1. List of 19 base images in early 2018 and 9 targeted images. Base images were used to detect slope displacements in targeted images.

19 base images in early 2018	5 target images in 2019
January: 11, 13, 16, 23, 28	
February: 5, 12, 17, 25	
March: 4, 9, 14, 19, 29	2019: 13-Apr., 17-Jul., 24-Aug., 5-
April: 3, 16, 23	Oct., 12-Nov.
May: 21	

June: 5

 Table 2. Eight periods (image pairs) were used to derive the Mindu slope movement.

Image pairs	Base image	Target image
#1	28 Oct. 2018	24 Nov. 2018
#2	24 Nov. 2018	23 Jan. 2019
#3	23 Jan. 2019	14 Mar. 2019
#4	14 Mar. 2019	18 May 2019
#5	18 May 2019	17 Jul. 2019
#6	17 Jul. 2019	28 Sep. 2019
#7	28 Sep. 2019	29 Nov. 2019
#8	29 Nov. 2019	07 Feb. 2020

Table 3. Detected image shifts (system error) in the "stable zone". The EW-std and NS-std indicates uncertainties of the method and the EW-mean and NS-mean were used to derive the final displacements in image pairs.

Image pairs	Dates	EW-mean	EW-std	NS-mean	NS-std	snr-mean	snr-std
#1	2015.11.13 2018.11.12	-0.495077	0.181026	-7.275188	0.253885	0.989819	0.001601
#2	2018.11.12 2019.11.12	4.115833	0.056559	9.914275	0.136149	0.989803	0.001434

305

310